Electrochemically Nanostructured Polyvinylferrocene/Polypyrrole Hybrids with Synergy for Energy Storage

Wenda Tian, Xianwen Mao, Paul Brown, Gregory C. Rutledge, and T. Alan Hatton**

Unconjugated redox polymers, such as polyvinylferrocene (PVF), have rarely been used for energy storage due to their low intrinsic conductivity. Conducting polymers with conjugated backbones, though conductive, may suffer from insufficient exposure to the electrolyte due to the often formed nonporous structures. The present work overcomes this limitation via simultaneous electropolymerization of pyrrole and electroprecipitation of PVF on electrode surfaces. This synthesis method relies on the π–π stacking interactions between the aromatic pyrrole monomers and the metallocene moieties of PVF. This fabrication process results in a highly porous polymer film, which enhances the ion accessibility to polypyrrole (PPy). PPy serves as a "molecular wire," improving the electronic conductivity of the hybrid and the utilization efficiency of ferrocene. The PVF/PPy hybrid exhibited a specific capacitance of 514.1 F g^{-1}, which significantly exceeds those of PPy (27.3 F g^{-1}) and PVF (79.0 F g^{-1}), respectively. This approach offers an alternative to nanocarbon materials for improving the electronic conductivity of polymer hybrids, and suggests a new strategy for fabricating nanostructured polymer hybrids. This strategy can potentially be applied to various polymers with π-conjugated backbones and redox polymers with metallocene moieties for applications such as energy storage, sensing, and catalysis.

1. Introduction

Driven by the staggering demands for sustainable and efficient energy storage solutions, extensive research efforts have focused on the furtherance of pseudocapacitors with high power density to bridge the gap between batteries and dielectric capacitors.[1,2] Instead of relying only on ion adsorption at the electrode surface, pseudocapacitors store charge via fast reversible surface/near-surface redox reactions, typical of electroactive materials such as metal oxides and conducting polymers.[2] Redox polymers with nonconjugated backbones such as polyvinylferrocene (PVF) are localized-state conductors[3–5] with discrete electron donor/acceptor sites. Electron hopping between neighboring redox centers on PVF, for instance, can induce redox reactions under an electrochemical stimulus. Despite its stable one-electron redox electrochemistry, flat charge/discharge profile, and electrochemical reversibility, PVF has not been widely reported as a medium for energy storage applications, for two reasons. First, the diffusion-like[6–9] electron transport mechanism in PVF renders a poor intrinsic conductivity of only 10^{-5}–10^{-7} S cm^{-1}.[10] Second, while close packing of polymers can increase the redox center concentration and hence reduce the intersite distance for fast electron hopping, it usually also results in a nonporous structure with limited polymer/electrolyte interface that hinders ion diffusion.[9] The compromise between electronic and ionic conductivity lowers the redox center utilization efficiency and makes it challenging to achieve the theoretical specific capacitance.[8] In only a handful of efforts to date have attempts been made to address this limitation, by incorporating conductive nanocarbon materials into PVF films. It was found that the introduction of dispersed graphite powders can increase the electronic conductivity of PVF-modified electrodes, with a resulting high charge capacity of 126.4 mAh g^{-1}.[11] Mao *et al.* combined carbon nanotubes with PVF to increase the utilization efficiency of ferrocene and achieved a specific capacitance of 418.8 F g^{-1}.[12] In contrast to PVF, whose nonconjugated backbone mainly serves as an insulated structural support, conducting polymers such as polypyrrole (PPy) allow charge transport along their extensively conjugated backbones via doping/de-doping.[4,13] In particular, PPy is electroactive over the redox potential range of PVF, with an intrinsic conductivity routinely above 10 S cm^{-1}.[10,14] Conducting polymers also offer great design flexibility and are easy to prepare, low cost, light weight, and sustainable.[15,16] With PPy as the conductive medium, neither surfactants nor additional sonication steps are required for dispersing precursors, such as graphite powders or carbon nanotubes prior to functionalization of the electrodes, which allows the fabrication process to be achieved in a single step, and to be readily scalable. However, a major limitation of using a bulk conducting polymer directly is insufficient exposure to the electrolyte solution due to the nonporous structure that is often formed. Previous efforts to engineer polymers into nanoporous structures have often involved multiple steps, where sacrificial materials used during polymerization are subsequently removed to introduce porosity.[17–22]

Here, we report a facile synthesis strategy for the preparation of a highly porous electroactive hybrid in which we exploit the π–π stacking interactions between pyrrole and the ferrocene

W. Tian, Dr. X. Mao, Dr. P. Brown,
Prof. G. C. Rutledge, Prof. T. A. Hatton
Department of Chemical Engineering
Massachusetts Institute of Technology
A77 Massachusetts Avenue, Cambridge, MA 02139, USA
E-mail: rutledge@mit.edu; tahatton@mit.edu

DOI: 10.1002/adfm.201501041

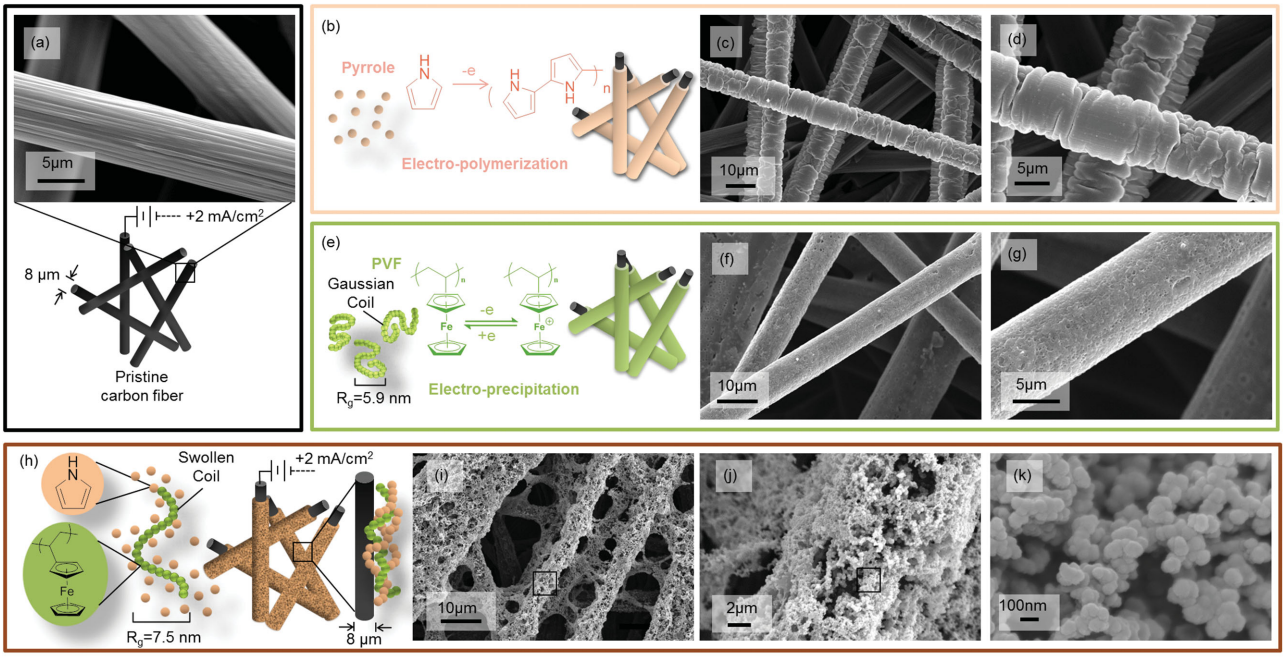

Figure 1. a) Schematic and SEM image of the pristine carbon fibers indicate their clean surfaces with striation patterns. b) Schematic and c,d) SEM images (different magnifications) of the electropolymerized pyrrole show the nonporous conformal coating of PPy films on each carbon fiber. e) Schematic and f,g) SEM images of the electroprecipitated PVF show that the formed PVF film had a rough and nonporous morphology. h) Schematic and i–k) SEM images of the codeposited coatings of PVF and PPy on carbon fibers demonstrate the highly porous film structure resulting from this fabrication method.

moieties of PVF. In this hybrid, PPy chains serve as molecular wires for the spatially isolated ferrocene moieties, increasing the utilization efficiency of ferrocene. PPy also increases the charge storage capacity via redox reactions in its bulk. This approach addresses the challenges to achieve a high specific capacitance with PVF, and offers an alternative to conventional nanocarbon materials for improving the electronic conductivity of polymer hybrids. This new strategy for fabricating nanoporous polymer hybrids via exploiting the intermolecular interactions between constituent molecules can potentially be applied to a variety of conducting polymers with π-conjugated backbones and redox polymers with various metallocene moieties.[23–25]

2. Results and Discussion

2.1. Morphological Characterization

Polymer-modified electrodes were fabricated with commercial carbon fiber papers as the substrate. Although limited in surface area compared to carbon nanofibers, commercial carbon fiber papers are convenient, provide a relatively greater surface area for polymer deposition as compared to flat sheets, and maintain a porous electrode architecture at a large scale. The various electrodes prepared in this work are identified using the nomenclature "substrate"-"deposited polymer;" for example, CF-PVF refers to electrodes comprising PVF deposited on carbon fibers (CF). For simplicity, CF-Codep refers to the electrodes comprising PVF and PPy codeposited on carbon fibers. Pristine carbon fibers showed clean surfaces with longitudinal striation patterns characteristic of Toray fibers (**Figure 1**a). Pyrrole in solution, upon oxidation, can undergo oxidative polymerization to form PPy (Figure 1b). The electrochemically polymerized PPy formed a segmented and densely grown film on each carbon fiber (Figure 1c,d). This morphology was consistent with the homogenous, closely packed, and globular-shaped structure of PPy reported previously.[26] Ferrocene units in PVF can be oxidized to ferrocenium under an appropriate electrochemical potential. The induced positive charge on ferrocenium increases the hydrophilicity of the polymer chain, driving PVF to precipitate onto the carbon fibers from the hydrophobic organic solvent (Figure 1e).[27] This electroprecipitated PVF coated each carbon fiber conformally and exhibited a nonporous, but relatively rough, morphology (Figure 1f,g). In contrast to the pure PVF or PPy polymer films, the polymer hybrid fabricated via simultaneous electrodeposition and electroprecipitation (Figure 1h) had a highly porous film structure (Figure 1i,j). This interconnected porous morphology was observed consistently throughout the entire carbon fiber framework (Figure 1i). A close examination via HR-SEM revealed that the codeposited film consisted of nanoscale polymeric spherical clusters with diameters of 50–100 nm (Figure 1k). These nanospheres adhered randomly to each other, forming an interconnected porous film with carbon fibers as the retaining framework. Within the polymer/carbon fiber composite, a dual scale porosity was observed, consisting of nanosized pores within the polymer film and micropores between the fibers. This morphology provided a large interfacial area between the polymer and the electrolyte, which facilitated diffusion of ions and rendered excellent electrochemical properties. To confirm

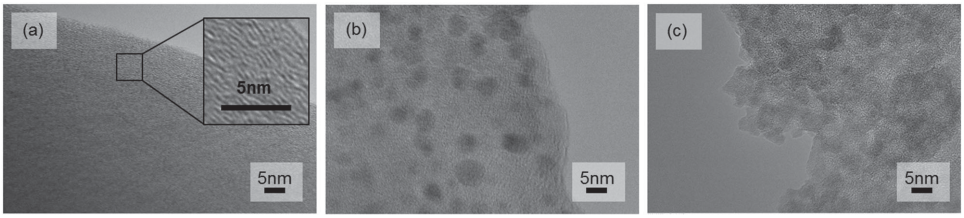

Figure 2. TEM images of electrochemically deposited a) PPy, b) PVF, and c) codeposited hybrid polymer film. The molar ratio of ferrocene to pyrrole units is about 5%–6%, based on composition of the deposition solution and confirmation by XPS (see text).

that this dual scale porous morphology was indeed a result of the codeposition process, sequentially deposited bilayer polymer films were fabricated. CF-PVF/PPy, with PVF as the inner layer and PPy as the outer layer, had a grainy and nonporous surface morphology, resulting from the thick outer layer of PPy (Figure S1a, Supporting Information). In comparison, the CF-PPy/PVF fabricated via the opposite order of deposition exhibited more roughness at the surface, while maintaining its dense film structure (Figure S1b, Supporting Information). The different morphological properties of the hybrid and bilayer polymer films were due to the two different electrodeposition processes, and motivated our detailed investigation of the codeposition process (see Section 2.6).

Transmission electron microscopy (TEM) was used to confirm the relatively uniform distribution of the ferrocene units within the codeposited hybrid film. **Figure 2**a shows the crystalline regions characteristic of pure PPy, the formation of which is attributed to the π–π interactions between adjacent PPy chains.[28] In pure PVF, the ferrocene moieties are observed as distinct black clusters with diameters ranging from 2 to 5 nm sitting atop a thin background layer of unclustered PVF (Figure 2b). In contrast to the morphologies of pure PPy and pure PVF, the crystalline regions and dark spheres are replaced by large gray areas in the codeposited polymer hybrid (Figure 2c). This morphological difference suggests that the ferrocene moieties were more homogenously distributed within the hybrid.

Nitrogen adsorption was used to characterize the pore structure of the codeposited polymer hybrid. The adsorption isotherm, or volume adsorbed versus relative pressure, P/P_0, where P_0 is the saturated vapor pressure, displayed a steep increase in slope at relative pressures above 0.8, and a hysteresis loop between the relative pressures of 1 and 0.8 on desorption (**Figure 3**a). This is a Type V isotherm according to the IUPAC classification, and indicates the presence of mesopores (2–50 nm) within the polymer hybrid[29] in which capillary condensation occurs at high P/P_0. The exhibited hysteresis is a result of the different pressures at which capillary condensation and capillary evaporation occur.[29] The specific surface area of the polymer hybrid obtained by the Brunauer–Emmett–Teller (BET) analysis is 166.8 $m^2\ g^{-1}$, which is significantly higher than values reported for pure polypyrrole (37–61 $m^2\ g^{-1}$),[30–33] such as polypyrrole porous clusters,[30] tubes,[30] nanoparticles,[30] and thin films,[33] or pure PVF powder (8 $m^2\ g^{-1}$).[12] The pore size distribution based on the Barret–Joyner–Halenda (BJH) theory (Figure 3b) displays a broad peak in the region of 5–80 nm, with an average of 26.0 nm and a maximum at 33.0 nm. This broad distribution of pore sizes is consistent with the combination of mesopores (2–50 nm) and macropores (>50 nm) observed in the polymer hybrid under SEM. This broad distribution of pore sizes can potentially enhance ion access to the electroactive polymers and improve the power capability of the hybrid.

2.2. Composition and Structure Characterizations

X-ray photoelectron spectroscopy (XPS) was performed to study the chemical composition of the polymer-modified electrodes. Fe_{2p} and N_{1s} signals served as elemental markers for PVF and PPy, respectively. An XPS survey scan of the codeposited polymer film indicated the presence of C_{1s}, O_{1s}, N_{1s}, Cl_{2p}, and Fe_{2p} through their photoelectron peaks in the polymer films, in contrast to the pristine carbon paper, where only a strong C_{1s} peak and a small O_{1s} peak were observed (**Figure 4**a). The existence of the Fe_{2p} and N_{1s} peaks confirmed the deposition of both PVF and PPy on the substrate. The presence of Cl_{2p} and the increased O_{1s} signal were due to the dopant, ClO_4^-, in PPy. The high-resolution N_{1s} spectrum was deconvoluted into a main peak at 399.8 eV and a second peak at 402.2 eV (Figure 4b). These two peaks corresponded to the neutral —NH— nitrogens and the oxidized C—N^+ nitrogens, respectively, indicating that the polymerized PPy was partially oxidized.[19,26,34] Fe_{2p} had two peaks from the spin-orbital splitting, $Fe_{2p,1/2}$ (721 eV) and $Fe_{2p,3/2}$ (708 eV), each of which was deconvoluted into two component peaks (Figure 4c). The two smaller component peaks of $Fe_{2p,1/2}$ and $Fe_{2p,3/2}$ at higher binding energies resulted from the partially oxidized ferroceniums.[35–37]

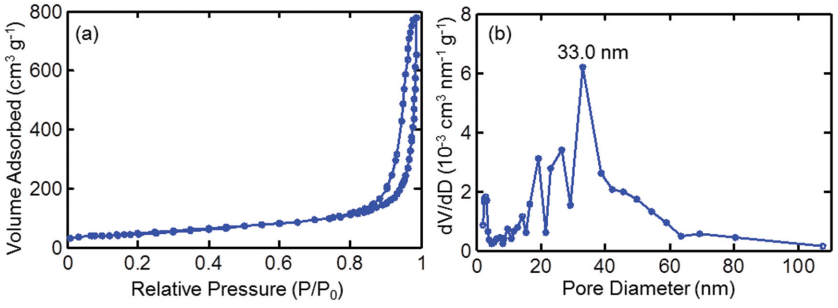

Figure 3. a) Nitrogen adsorption–desorption isotherms of the PVF/PPy polymer hybrid. b) The corresponding BJH pore-size distribution for the polymer hybrid.

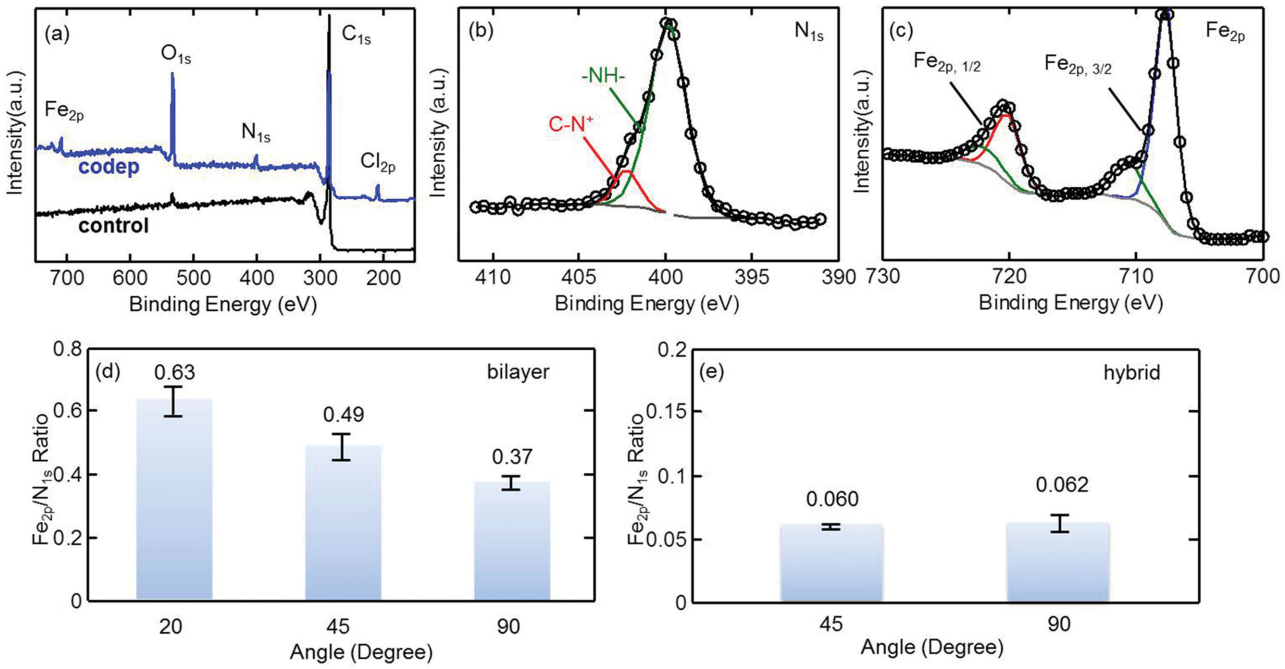

Figure 4. a) Survey scans of the pristine carbon fiber paper (control) and codeposited polymer hybrid indicate the presence of C_{1s}, O_{1s}, N_{1s}, Cl_{2p}, and Fe_{2p}. High resolution scans of b) N_{1s} and c) Fe_{2p}. d,e) Fe_{2p}/N_{1s} ratios obtained from angle-resolved XPS for CF-PPy/PVF bilayer and hybrid films, respectively, deposited on flat stainless steel sheets. The bilayer film shows a decreasing iron content with increasing depth, while a uniform distribution of ferrocene moieties within the codeposited hybrid films was observed.

Angle-resolved XPS was used to probe the differences in depth profiles of chemical composition between sequentially deposited and codeposited polymer films. Since the local angle at the surface of a polymer-modified carbon fiber is difficult to determine and can be different from that of the sample holder relative to the XPS analyzer, we performed the angle-resolved XPS tests on polymer hybrid films deposited directly onto flat stainless steel sheets. The depth at which the composition was detected increased as the tilt angle increased. The peak intensity was used to obtain the relative atomic concentration of each element. The Fe_{2p}/N_{1s} ratio, which measures the ratio of ferrocene to pyrrole units in the polymer hybrid, decreased with increasing tilt angles from 20° to 90°, indicating that more PVF was deposited at the outer surface than in the inner layer of the polymer film for the PPy/PVF bilayer polymer film (Figure 4d). In the codeposited polymer film, the ratio remained approximately the same throughout the analyzed depth, indicating that PVF was distributed uniformly within the polymer hybrid (Figure 4e). This observation is consistent with the conclusions drawn from TEM images. It is worth noting that, in the codeposited polymer hybrid, the Fe_{2p} content was only ca. 6% of that of N_{1s}. This was consistent with the composition of the deposition solution, where the ratio of the molar concentration of ferrocene units to pyrrole monomer was ca. 5%.

2.3. Electrochemical Characterization in Three-Electrode Systems

The interesting morphologies of the PVF/PPy hybrids show promise for energy storage applications. First, we evaluated the electrochemical properties of the hybrids in three-electrode systems. The cyclic voltammetry (CV) profiles in **Figure 5**a indicate that the carbon fiber substrate contributed negligibly to the capacitance, while the electrochemically polymerized PPy film exhibited a quasirectangular CV curve within the voltage window of 0–0.7 V. This featureless profile resulted from the successive surface redox reactions of PPy films, indicating the perfect electrochemical capacitive behavior typical of PPy.[16,38] In contrast, the deposited PVF film exhibited distinct oxidation and reduction peaks at 0.35 and 0.25 V, respectively.[11,27] The CV curve for CF-PPy/PVF comprises both the broad quasirectangular profile from PPy and the pronounced anodic/cathodic peaks from PVF, indicating that PVF and PPy were both electroactive in the hybrid (Figure 5b). PPy as the inner layer was able to transport electrons effectively to the outer film of PVF, allowing two well-defined redox peaks similar to those in the pure PVF films to develop. By contrast, the redox peaks in CF-PVF/PPy are barely discernible, presumably because the dense PPy outer layer limited ion diffusion to the ferrocene moieties in the inner layer (Figure 2b). CF-Codep displayed strong PVF redox peaks, and gave a much higher current response than did the other electrodes. The significant increase in the contributions of both polymer components to the specific capacitance indicated that the utilization efficiency of ferrocene and the ion accessibility to PPy were simultaneously improved upon forming the hybrid. The PVF/PPy hybrid also exhibited excellent rate performance. The specific capacitance of CF-Codep was much higher than that of the other electrodes, within the scan rate range of 0.001–0.2 V s^{-1}, and remained at ≈200 F g^{-1} even at 0.2 V s^{-1} (Figure 5c).

The excellent electrochemical properties of the polymer hybrids were also evident in the galvanostatic discharge profiles (Figure 5d). The discharge profile of PVF exhibited a

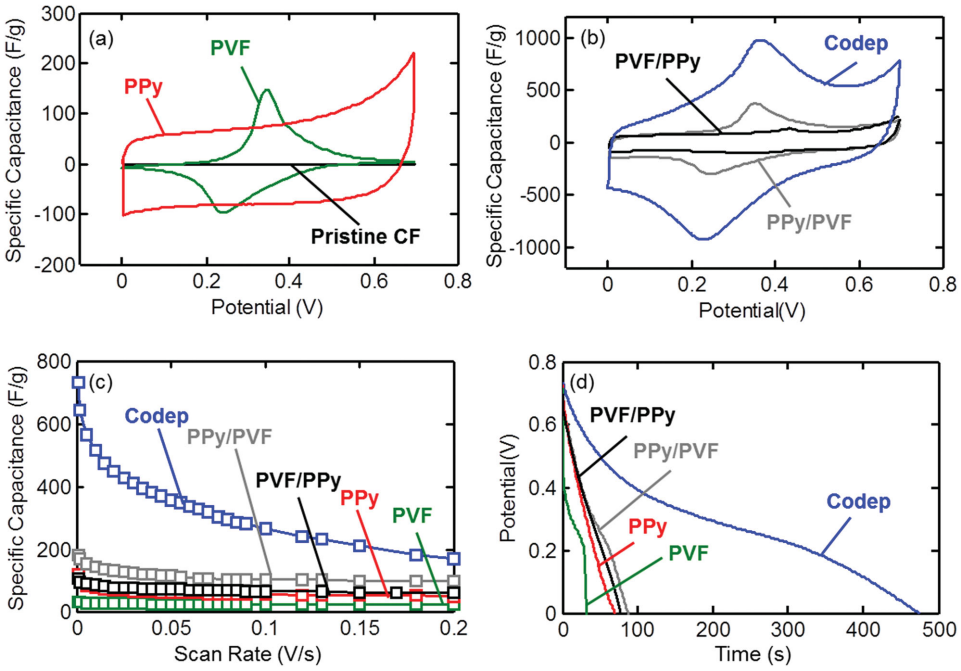

Figure 5. a) The CV profiles of PPy and PVF compared to that of pristine carbon fibers. b) The cyclic voltammetry profiles indicate the codeposited polymer films gave a higher current response than the sequentially deposited polymer films. c) The codeposited polymer film shows better rate performance at various scan rates of 0–0.2 V s^{-1}. d) The galvanostatic discharge curves for various polymer modified electrodes at a current density of 1 A g^{-1}.

sudden decrease in potential at short time (<1 s), followed by an extended period (up to 30 s) where the potential decreased more slowly, as a result of the reduction of the ferrocenium to ferrocene. Upon complete reduction of all the ferrocenium units, the potential quickly plunged to zero.[11] In contrast, the curve for PPy was more linear, with no significant decrease in slope. This behavior arises because PPy has no defined redox potential within the potential window used, consistent with its featureless quasirectangular CV profile (Figure 5a). Both the bilayer (CF-PVF/PPy and CF-PPy/PVF) and the hybrid films deviated from a linear profile, with a decrease in the rate of change of potential at around 0.25 V. This "flattening" of the potential profile was a result of the redox reactions of the ferrocene centers. It is clear that the discharge profiles of the hybrid systems exhibited the characteristics of both PVF and PPy, but that the hybrid film displayed a much broader discharge profile than did the bilayer films, indicating a much larger charge storage capacity. A similar trend in charge storage capability was also observed in the comparison of CV profiles in Figure 5b.

Electrochemical storage capacity relies on the utilization efficiency of the redox units. In CF-PVF/PPy, PVF was deposited directly on the carbon fiber, beneath the densely grown PPy layer (Figure 2a); thus ions in the electrolyte had limited access to the PVF, which then could not be fully oxidized. This limitation manifested itself in the suppressed redox peaks in the CV profile (Figure 5b). In addition, the electron transport between PPy and the carbon fiber substrate was also compromised in this system, because the PVF backbone served mainly as an insulating structural support and so electron transport occurred only by hopping of the electrons between the neighboring ferrocene centers. PVF permitted limited electron access to the outer-layer PPy, and thus the charge storage sites along the PPy chains were not utilized efficiently; this inefficiency ultimately resulted in the relatively low overall capacitance of 103.2 F g^{-1}. Though the ion diffusion limitation within CF-PPy/PVF was still expected, the inner polymer layer of PPy was conductive and could facilitate electron transport to the PVF. Therefore, CF-PPy/PVF exhibited the relatively higher specific capacitance of 144.1 F g^{-1}. The enhanced electrochemical performance of the codeposited hybrid, as manifested by its specific capacitance of 514.1 F g^{-1}, was realized via the synergy between PVF and PPy. The charge delocalization along the backbone of PPy complemented the electron hopping between the redox moieties within the formed hybrid. Thus, PPy chains served as "molecular wires" providing fast electron access to the isolated ferrocene moieties, which then could be efficiently oxidized and reduced. The highly porous nanostructure also increased the electrolyte–electrode interfacial contact area and ensured a high ionic conductivity by allowing easier ion diffusion within the films and facilitating the counterion insertion/extraction during the doping/dedoping of PPy and the redox reactions of the ferrocene moieties.

In addition, we also compared the performance of the PVF/PPy hybrid with a broad range of alternative supercapacitor electrode materials for energy storage applications, such as porous carbons and various inorganic electroactive species (Table S1, Supporting Information). This comparison shows that the PVF/PPy hybrid has a higher specific capacitance than most of the recently reported carbon-based supercapacitor materials, such as corncob-residue-derived carbon,[39] nitrogen-containing carbon microspheres,[40] etc. This is due to the pseudocapacitance contribution from both PVF and PPy. Compared to the recently reported transition metal oxide/porous carbon composite materials,[41–43] the PVF/PPy hybrid

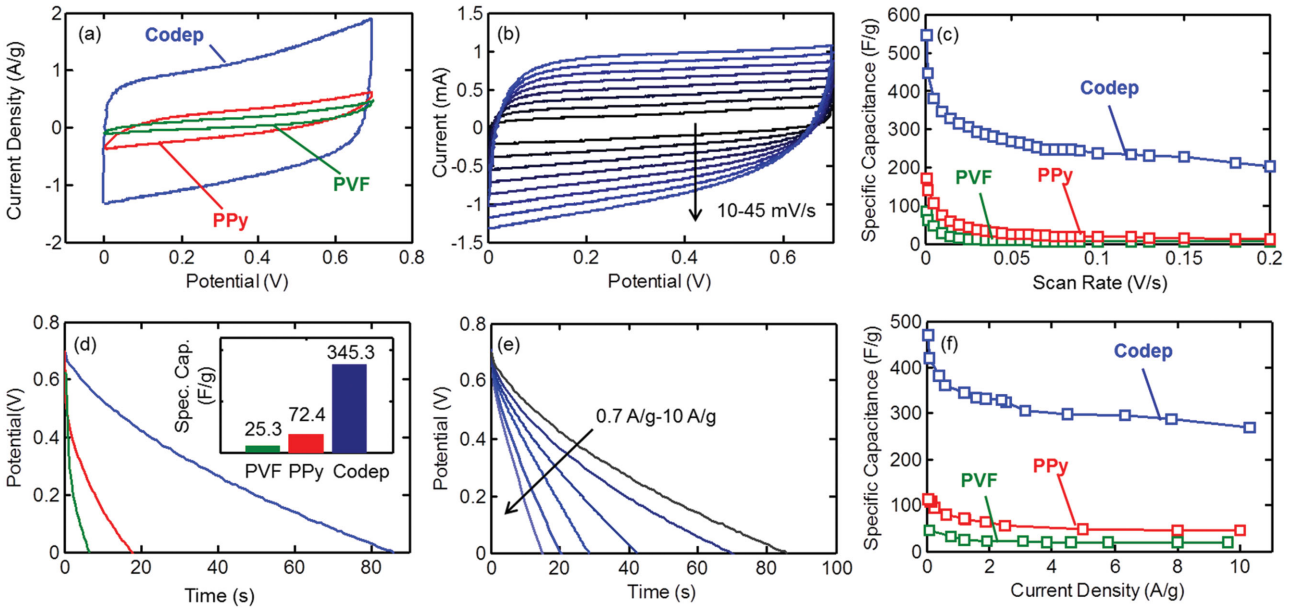

Figure 6. Electrochemical evaluation of the two-electrode configuration: a) CV profiles for PPy, PVF, and the codeposited hybrid. b) CV profiles for the codeposited hybrid at scan rates from 10 to 45 mV s^{-1}. c) The calculated specific capacitance at scan rates from 0.001 to 0.2 V s^{-1}. d) The galvanostatic discharge curves recorded at 0.7 A g^{-1} and the calculated specific capacitance. e) The galvanostatic discharge curves of the codeposited PVF/PPy hybrid at current densities from 0.7 to 10 A g^{-1}. f) The calculated specific capacitance of PVF, PPy, and the codeposited hybrid at current densities from 0.06 to 10 A g^{-1}.

has a comparable or slightly higher specific capacitance. Different from metal oxide/carbon composites, the PVF/PPy hybrid is fabricated from a facile electrochemical codeposition method, which can potentially be generalized to various other metallocene-containing polymers and conducting polymers. In addition, the hybrid polymer film can also be combined with various carbon nanomaterials, such as carbon nanotubes or graphene, to further improve its properties.

2.4. Two-Electrode Symmetric Supercapacitor Device Performance

We also assessed the polymer hybrids in a two-electrode system that resembles the physical configuration in, and the operating conditions of, commercial packaged supercapacitors; our purpose in doing so was to provide a more meaningful measure of the material's performance for commercial applications.[44–46] **Figure 6**a compares the CV profiles of PVF, PPy, and the codeposited PVF/PPy hybrid. The codeposited hybrid gave a much larger current response than did the PVF and PPy films, and displayed a quasirectangular CV profile. The disappearance of redox peaks in the two-electrode configuration is commonly seen in electroactive polymers, for reasons that are as yet unclear.[44,45] As the scan rate increased, the CV profiles for the codeposited hybrid showed slight distortions from the quasirectangular shape, due to the increasing overpotential from the ion transport within the polymers (Figure 6b). The galvanostatic discharge curves (Figure 6d,e) indicated the much higher charge storage capacity of the hybrid polymer compared to those of pure PVF and pure PPy films. The calculated specific capacitance at various scan rates from 0.001 to 0.2 V s^{-1} and at various current densities from 0.06 to 10 A g^{-1} demonstrated the excellent rate performance of the codeposited polymer film in the two-electrode cell (Figure 6c,f). The codeposited PVF/PPy hybrid exhibited a specific capacitance of 345.3 F g^{-1}, which is significantly higher than that of either PVF or PPy (Figure 6e).

To gain further insight into the advantages of the codeposited hybrid structure, electrochemical impedance spectroscopy (EIS) measurements were conducted on the two-electrode supercapacitor cells; the resulting Nyquist plots for CF-PVF, CF-PPy, and CF-Codep are shown in **Figure 7**a. Compared to CF-PVF or CF-PPy, CF-Codep exhibited a lower solution resistance (R_s, determined by the intercept on the Z_{re}-axis) and a lower interfacial charge transfer resistance (R_{ct}, indicated by the diameter of the charge transfer semicircle or the length of the Warburg region).[47] Such decreases in R_s and R_{ct} further suggest that the ion diffusion resistance was reduced because of the formation of a porous structure and enhanced electron transport properties that result from incorporation of the conducting polymer component. The Coulombic efficiency was calculated to be 99.5% for the codeposited polymer hybrid at a current density of 5 A g^{-1}. The power and energy densities determined from galvanostatic charge/discharge measurements in a two-electrode system are given in the Ragone plot shown in Figure 7b. This capacitor cell was characterized by a high energy density of 40.7 W h kg^{-1} at a power density of 6.79 kW kg^{-1}; the energy density decreased by only about 40% to 25.4 W h kg^{-1} following a significant ninefold increase in the power density to 58.6 kW kg^{-1}. This enhanced power density at the expense of a relatively small decrease in energy density is attributed to the facilitated ion diffusion within the porous polymer films. The achieved maximum energy density is comparable to that of lead acid batteries (25–40 W h kg^{-1})[48] and much higher than that of activated carbon-based supercapacitors (4–5 W h kg^{-1}).[49]

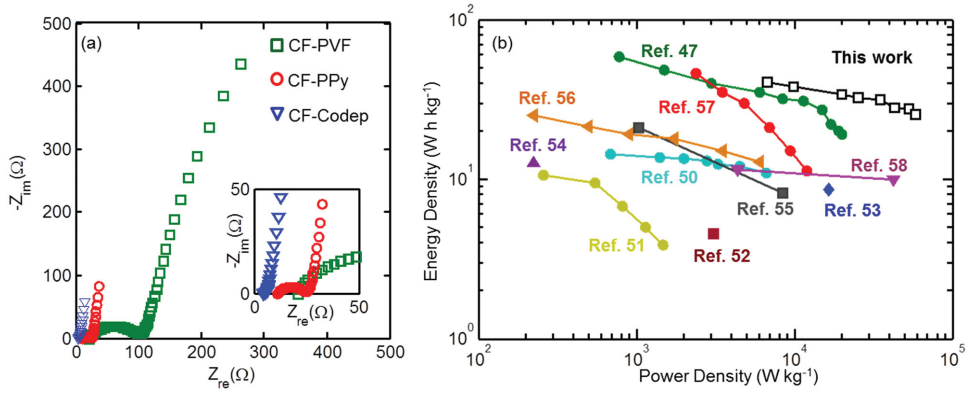

Figure 7. a) Nyquist plots for CF-PVF, CF-PPy, and CF-Codep indicate lower solution and interfacial charge transfer resistances for the codeposited polymer hybrids. b) Ragone plot for the PVF/PPy polymer hybrid-based two-electrode symmetric supercapacitor performance relative to that of other conducting polymer-based supercapacitors reported in literature.[47,50–58]

Compared to some of the recently reported conducting polymer-based supercapacitor devices,[47,50–58] the PVF/PPy hybrid-based supercapacitor gives a higher energy density due to the additional pseudocapacitance offered by PVF.

2.5. Cycling Stability

Conducting polymers usually have limited cycling stabilities due to repeated volumetric swelling and shrinking during charging/discharging.[2,59] The volume change and the resulting mechanical stress often lead to mechanical degradation and dissolution of polymer films,[60–62] as was also observed in the PVF/PPy polymer hybrid in this study. To address this cycling degradation issue, we utilized a hydrothermal process to deposit a thin layer of carbonaceous material on each of the hybrid clusters to mitigate the effects of the swelling and deswelling of the material during cyclic charging/discharging process.[59] In the hydrothermal process, glucose was converted under mild conditions to a nanometer-thick carbon shell coating the materials.[63–66] This method has been used to improve the stability of conducting polymers and metal oxides without compromising their electrochemical performance.[64,67] The porous structure of the polymer hybrid was maintained during the hydrothermal coating process as observed by SEM, BET surface area, and pore size distribution (Figure S3a,b,d,e, Supporting Information). XPS analysis on the PVF/PPy hybrid after the hydrothermal process indicated the presence of the carbon coating on the polymer surface (Figure S3g, Supporting Information). **Figure 8**a compares the CV curves for the PVF/PPy hybrid observed in a three-electrode system before and after the hydrothermal treatment. The deposition of the thin carbon shell resulted in a distorted CV profile, but with a slight increase in the capacitance due to the increased double layer effect from the carbon shells. EIS results and the calculated specific capacitance from both the CV and galvanostatic measurements (Figure S3f,h–j, Supporting Information) confirmed that the electrochemical performance was not compromised by the hydrothermal process. The polymer hybrid retained 94.5% of its specific capacitance after 3000 cycles at 5 A g^{-1} (Figure 8b), and exhibited minor changes in its surface morphology after the cycling evaluation (Figure S3c, Supporting Information).

2.6. Molecular Interactions between Ferrocene and Pyrrole

The different surface morphology and enhanced electrochemical properties of the polymer hybrid relative to the sequentially deposited components was due to the influence of intermolecular interactions between the PVF and pyrrole molecules on the

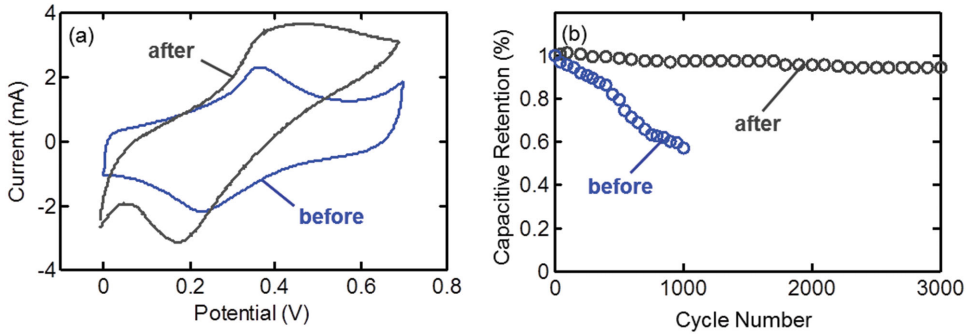

Figure 8. a) The PVF/PPy hybrid electrode exhibits a more distorted CV profile after the hydrothermal process compared to that of the untreated electrode. b) The cycling stability of the PVF/PPy hybrid modified electrode is significantly improved following the hydrothermal treatment, with retention of 94.5% of its specific capacitance at 5 A g^{-1} after 3000 cycles.

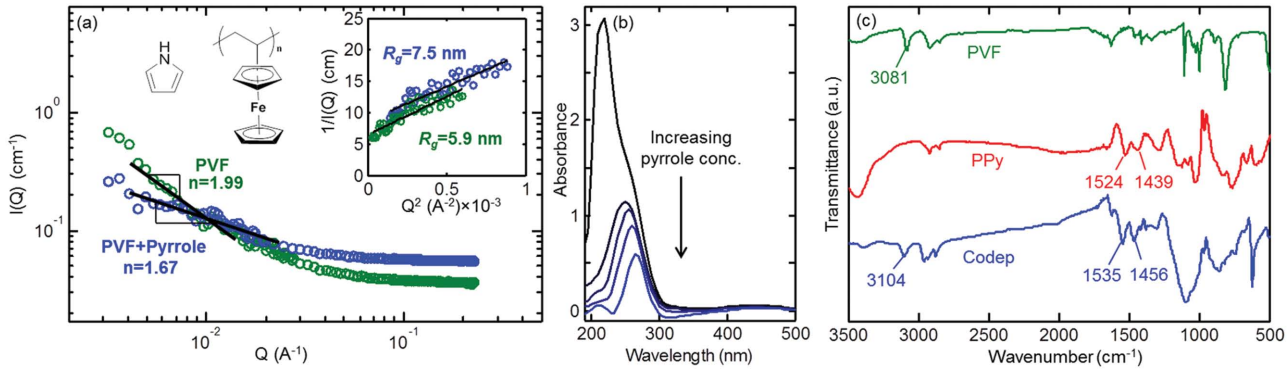

Figure 9. a) SANS profiles of PVF with (blue) and without (green) pyrrole indicate the conformation change of PVF chains in solution. Inset: Partial Zimm plots of PVF and PVF in the presence of pyrrole. b) UV–vis absorbance of 0.3×10^{-3} M ferrocene in ethanol decreased significantly as the concentration of pyrrole increased from 0 to 100×10^{-3} M. c) FTIR of PVF, PPy and the formed hybrid indicated the red-shift of peaks for C═C stretching and C—N stretching in the pyrrole ring and the C—H stretching in the ferrocene moieties.

simultaneous electropolymerization and electroprecipitation process. In the codeposition solution, each PVF polymer chain was solvated partially by pyrrole because PVF-pyrrole interactions are more favorable than those between PVF and $CHCl_3$ due to the π–π stacking interactions. Upon electrodeposition of the swollen PVF coils, the solvating pyrrole molecules were in a position to be electropolymerized to form polypyrrole; the PVF molecules were incorporated into and intimately associated with the PPy in the resulting film. The change in PVF polymer chain conformation in solution prior to deposition due to its interaction with pyrrole was revealed using small-angle neutron scattering (SANS) and UV–vis absorbance spectrometry. This intimate interaction between the two polymers within the formed hybrid was further elucidated via Fourier transform infrared spectroscopy (FTIR).

2.6.1. Small-Angle Neutron Scattering (SANS)

Small-angle neutron scattering (SANS) was used to probe the conformation of the PVF polymer chains in solution. It is evident from the two different SANS profiles (scattering intensity $Q = (2\pi / \lambda)\sin(2\theta)$, where θ is the scattering angle, and λ is the radiation wavelength) shown in **Figure 9** that PVF underwent conformational changes in the presence of pyrrole. Porod analysis confirmed this change by yielding information on the "fractal dimension" of the polymer coil.[68] In the high-Q region, the intensity was approximated as

$$I(Q) = \frac{A}{Q^n} + B \tag{1}$$

For polymer coils, the Porod slope n was extracted by plotting log (I (Q)–B) versus log (Q) (Figure 9), where B is the background. The exponent n is related to the excluded volume parameter ν by $n = 1/\nu$; Gaussian, swollen, and collapsed coils have Porod slopes of 2, 5/3, and 3, respectively. For PVF in chloroform, we extracted an n value of 1.99, which is consistent with θ conditions for the solution ($\nu = 0.5$) and the Gaussian coil. However, when PVF was combined with pyrrole, n was found to be 1.67, indicating a transformation into swollen coils. This change in chain conformation was attributed to interactions between the PVF coils and pyrrole monomers, presumably through the π–π stacking. In this way, pyrrole monomers extended the PVF chains in solution, swelling the PVF coil. An increase in the measured radius of gyration (R_g) again confirmed the structural change of PVF in solution. To obtain R_g for the polymer, partial Zimm plots were prepared (Figure 9 inset).[68] Here, a Lorentzian form for the Q-dependence of the scattering intensity was assumed

$$I(Q) = \frac{I_0}{1 + Q^2\xi^2} \tag{2}$$

where ξ represents the correlation length, and is proportional to the Flory–Huggins interaction parameter. In the low-Q region, it can be used to estimate R_g

$$\xi = \frac{R_g}{\sqrt{3}} \tag{3}$$

In chloroform R_g for PVF was estimated to be 5.9 nm, and increased by about 30% to around 7.5 nm when pyrrole monomers were present in solution.

2.6.2. UV–Vis Spectroscopy

To substantiate the likelihood of the π–π stacking interactions between PVF and PPy, we used UV–vis spectroscopy to probe the molecular interactions between pyrrole monomer and PVF, both of which possess π-aromatic cyclic moieties, in solution. The ferrocene units in each repeating unit of PVF contain two cyclopentadiene rings and have a characteristic energy absorption band around 220 nm, corresponding to the $\pi \rightarrow \pi^*$ transition.[69] Each pyrrole molecule contains a five-membered heterocyclic aromatic ring, exhibiting a characteristic peak around 210 nm.[70] For simplicity, the UV–vis spectrum of ferrocene was studied, rather than that of PVF, along with the spectrum of pyrrole. The ferrocene absorption peak decreased significantly as the pyrrole concentration increased from 0×10^{-3} M to 100×10^{-3} M (Figure 9b). The decreased UV absorption intensity, or hypochromism, of ferrocene in the presence of pyrrole is commonly observed in molecules with

π–π stacking interactions, which is a result of the intermolecular overlapping of *p*-orbitals in their π-conjugated systems.[71] This significant suppression of the ferrocene absorption peak indicates intimate molecular interactions between pyrrole and ferrocene in solution, which could be a result of a greatly extended molecular packing between the cyclopentadiene rings in PVF and the heterocyclic aromatic ring in pyrrole.[71]

2.6.3. Fourier Transform Infrared Spectroscopy (FTIR)

SANS and UV–vis spectroscopy elucidated the molecular interaction between pyrrole and PVF in solution before the electrochemical codeposition. We used FTIR to study this interaction within the formed hybrid after the codeposition process. Pure PVF shows characteristic peaks at 3081, 1105, 1023, 999, and 810 cm^{-1} (Figure 9c).[69] For electrochemically polymerized PPy, FTIR shows characteristic peaks at 1524, 1439, 1080, and 1012 cm^{-1}.[72] In comparison, the codeposited polymer hybrid exhibited a broad peak from 1000 to 1300 cm^{-1}, as a result of the overlap of the peaks from the PVF and the significantly higher content of PPy in the hybrid. However, the peak corresponding to the C—H stretching of the ferrocene units[73] shifted from 3081 to 3104 cm^{-1} in the hybrid compared to the pure PVF. Similarly, the two observed peaks at 1524 cm^{-1} (C=C stretching) and 1439 cm^{-1} (C—N stretching) in PPy shifted to 1535 and 1456 cm^{-1} in the hybrid, respectively. This red-shift of peaks for the C=C stretching and C—N stretching in the pyrrole ring and the C—H stretching in ferrocene indicated that the interactions between π-electrons of the cyclopentadiene rings and the pyrrole still exist within the formed hybrid.[73]

2.6.4. Hybrid Film Structure Formation

The electropolymerization of pyrrole starts with the oxidation of pyrrole monomers at the electrode surface to form cation radicals, followed by dimerization. Further oxidation of the dimers induces polymer chain growth, which occurs simultaneously with the formation of oligomers in solution.[22] The nucleation of PPy on the electrode surfaces occurs when the length of the oligomeric chains surpasses the solubility limit. Here, the ferrocene groups of PVF, which are known to be associated closely with the pyrrole monomer in solution, may work as electron transfer mediators[74,75] to facilitate the formation of the pyrrole cation radicals and pyrrole oligomers in the vicinity of these PVF chains. We hypothesize that a mesoscopic phase separation occurs between the chloroform-rich phase and the pyrrole/oligopyrrole-rich phase as pyrrole monomers polymerize, with PVF partitioning preferentially into the pyrrole/oligopyrrole-rich phase, to contribute to the formation of the highly porous morphology. Although the exact mechanism of the porous film formation still remains unclear, preliminary results with other conducting polymer monomers that can have π–π stacking interactions with PVF indicate that this synthesis strategy can be generalized. We have electrochemically codeposited PVF/polyindole hybrid and PVF/polyaniline hybrid. The surface morphologies of these hybrid films (Figure S4b,d, Supporting Information) are significantly more porous than those of the electrochemically polymerized pure polyindole and pure polyaniline films (Figure S4a,c, Supporting Information). Further examination of these analogous systems is the subject of ongoing research.

3. Conclusion

We report a facile approach to synthesize a highly porous electroactive polymer hybrid with enhanced electrochemical energy storage performance. The synthesis strategy involved simultaneous electropolymerization of pyrrole and electroprecipitation of PVF. The π–π stacking interactions between the heterocyclic pyrrole and the cyclopentadiene rings in ferrocene units cause the PVF coil to swell in solution. These pyrrole monomers are believed to remain associated with the PVF coils upon their electropolymerization. As a result, the two polymers are codeposited on the substrate during the polymerization of PPy, such that the PPy chains interpenetrate the PVF domains and the two components are intimately associated with each other within the film thus formed. The polymer hybrid constructed in this way exhibited a highly porous morphology that is likely due to a phase separation between the pyrrole/oligopyrrole-rich and chloroform-rich phase during the polymerization process. This hybrid demonstrated excellent electrochemical properties, directly arising from the synergistic effects between PPy and PVF. A specific capacitance of 514.1 F g^{-1} was achieved for the PVF/PPy hybrid, which was significantly higher than those of PPy (27.3 F g^{-1}) and PVF (79.0 F g^{-1}). This facile electrochemical codeposition approach can potentially be used to fabricate flexible supercapacitor devices. This interesting combination of properties from conducting polymers and nonconducting redox polymers with metallocene moieties opens up new opportunities for the design and fabrication of porous polymer hybrids with synergy for a variety of applications, such as energy storage, sensing, and catalysis.

4. Experimental Section

Electrode Fabrication: Polymer modified electrodes were prepared by applying a constant current density of 2 mA cm^{-2} to the carbon paper electrode in a three-electrode cell, where the counter electrode was a Pt wire and the reference electrode was Ag/AgCl. The PVF/PPy hybrids were fabricated by electrochemical codeposition in 5 mL chloroform ($CHCl_3$) solution containing 0.104 M pyrrole, 1 mg mL^{-1} PVF, and 0.1 M tetrabutylammonia perchlorate (TBA-ClO_4). All depositions were performed for 5 min.

Electrochemical Characterization: All electrochemical polymerization and electrochemical characterizations were performed using an AutoLab PGSTAT 30 potentiostat and GPES software, version 4.9 (Eco Chemie). Cyclic voltammetry and galvanostatic discharge measurements were conducted in 0.5 M sodium perchlorate solution in both the three-electrode system and the two-electrode system. In the three-electrode cell, Pt wire and Ag/AgCl were used as the counter electrode and the reference electrode, respectively. The two-electrode cell was fabricated by sandwiching a filter paper between two polymer-deposited carbon paper electrodes. The electrode-filter paper-electrode set-up was then inserted between two glass slides for support. The electrochemical impedance spectroscopy (EIS) measurements on the two-electrode supercapacitor cells were performed in the frequency range of 100 kHz to 0.01 Hz with an electrochemical impedance analyzer (Gamery EIS300TM).

Polymer Characterization: Nitrogen adsorption/desorption was conducted on an automatic volumetric adsorption analyzer (Micromeritics ASAP2020). The PVF/PPy polymer hybrid films were first deposited on stainless steel sheets and then peeled off for the N_2 physisorption measurements. XPS was performed with a PHI Versa Probe II. The X-ray used was set at 200 μm, 50 W, and 15 kV. An XPS full scan survey was performed with a pass energy of 187.85 eV in the 0–1100 eV binding energy region. Angle-resolved XPS was performed with an argon single-ion gun for depth profiling. Changes in elemental composition within the polymer films up to 10 nm in depth were recorded nondestructively at various sample tilt angles relative to the analyzer, with values of 20°, 45°, and 90°. To allow depth profiling, the angle-resolved XPS was performed on polymer hybrid films that were deposited on a flat stainless steel sheet in the absence of carbon fibers. XPS survey scans were analyzed using the CasaXPS software. The spectra were calibrated with the C_{1s} peak (284.8 eV). The quantification regions are subtracted using a Shirley background. Small-angle neutron scattering (SANS) was performed on the D22 diffractometer at Institut Laue-Langevin, Grenoble, France. The neutron wavelength used was $\lambda = 10$ Å at two different detector distances and a Q value between 0.0024 and 0.37 $Å^{-1}$ was realized. The absolute cross section $I(Q)$ (cm^{-1}) as a function of momentum transfer Q ($Å^{-1}$) was obtained via data normalization. The measurements were performed in Hellma-fused silica cuvettes with a path length of 2 mm. To provide the necessary contrast, the dilute polymer aqueous systems were measured at 5 mg mL^{-1} in D-chloroform (scattering length density $\rho = 3.11 \times 10^{10}$ cm^{-2}). Data analyzed were in absolute units based on the sample compositions. A flat background term was employed to account for any low level of residual incoherent scattering during the fitting process. UV–vis absorption experiments were performed with Evolution201/220 UV–visible Spectrophotometers (Thermo Scientific). Fourier transform infrared spectroscopy (FT-IR) was measured on Nicolet NEXUS. Thermogravimetric analysis of the prepared electrodes was conducted using Q50 TGA (TA Instruments). Samples were equilibrated at room temperature, followed by ramping from room temperature to 900 °C at a heating rate of 5 °C min^{-1}.

Supporting Information

Supporting Information is available from the Wiley Online Library or from the author.

Acknowledgements

This research was supported by a grant from the MIT Energy Initiative Seed Fund program. X.M. was supported by a Skoltech Fellowship. This work made use of the Cornell Centerfor Materials Research Shared Facilities which are supported through the NSF MRSEC program (DMR-1120296).

Received: March 16, 2015
Revised: May 7, 2015
Published online: June 24, 2015

[1] A. S. Arico, P. Bruce, B. Scrosati, J. M. Tarascon, W. Van Schalkwijk, *Nat. Mater.* **2005**, *4*, 366.
[2] P. Simon, Y. Gogotsi, *Nat. Mater.* **2008**, *7*, 845.
[3] *Modern Aspects of Electrochemistry No. 44*, Vol. *44*, Springer, New York **2009**.
[4] G. Inzelt, *Conducting Polymers*, Springer, Berlin **2012**.
[5] *Advances in Chemical Physics: Polymeric Systems*, Vol. *94*, John Wiley & Sons, Inc., Hoboken, NJ, USA **1996**.
[6] J. M. Savéant, *J. Electroanal. Chem. Interfacial. Electrochem.* **1986**, *201*, 211.
[7] E. Laviron, *J. Electroanal. Chem. Interfacial. Electrochem.* **1980**, *112*, 1.
[8] M. A. Vorotyntsev, S. V. Vasilyeva, *Adv. Colloid Interface Sci.* **2008**, *139*, 97.
[9] E. F. Dalton, N. A. Surridge, J. C. Jernigan, K. O. Wilbourn, J. S. Facci, R. W. Murray, *Chem. Phys.* **1990**, *141*, 143.
[10] W. H. Smyrl, M. Lien, in *Applications of Electroactive Polymers* (Ed: B. Scrosati), Springer, London **1993**, p. 29.
[11] C. Iwakura, T. Kawai, M. Nojima, H. Yoneyama, *J. Electrochem. Soc.* **1987**, *134*, 791.
[12] X. Mao, F. Simeon, D. S. Achilleos, G. C. Rutledge, T. A. Hatton, *J. Mater. Chem. A* **2013**, *1*, 13120.
[13] J. Janata, M. Josowicz, *Nat. Mater.* **2003**, *2*, 19.
[14] G. A. Snook, P. Kao, A. S. Best, *J. Power Sources* **2011**, *196*, 1.
[15] O. Bubnova, Z. U. Khan, H. Wang, S. Braun, D. R. Evans, M. Fabretto, P. Hojati-Talemi, D. Dagnelund, J.-B. Arlin, Y. H. Geerts, S. Desbief, D. W. Breiby, J. W. Andreasen, R. Lazzaroni, W. M. Chen, I. Zozoulenko, M. Fahlman, P. J. Murphy, M. Berggren, X. Crispin, *Nat. Mater.* **2014**, *13*, 190.
[16] M. Zhou, J. Qian, X. Ai, H. Yang, *Adv. Mater.* **2011**, *23*, 4913.
[17] R. G. Northcutt, V. B. Sundaresan, *J. Mater. Chem. A* **2014**, *2*, 11784.
[18] M. S. Kim, J. H. Moon, P. J. Yoo, J. H. Park, *J. Electrochem. Soc.* **2012**, *159*, A1052.
[19] D. Kowalski, P. Schmuki, *Chem. Commun.* **2010**, *46*, 8585.
[20] P. N. Bartlett, P. R. Birkin, M. A. Ghanem, C. S. Toh, *J. Mater. Chem.* **2001**, *11*, 849.
[21] J.-Y. Kim, K. H. Kim, K. B. Kim, *J. Power Sources* **2008**, *176*, 396.
[22] J. I. Lee, S. H. Cho, S. M. Park, J. K. Kim, J. K. Kim, J. W. Yu, Y. C. Kim, T. P. Russell, *Nano Lett.* **2008**, *8*, 2315.
[23] Y. Yan, J. Y. Zhang, Y. L. Qiao, M. Ganewatta, C. B. Tang, *Macromolecules* **2013**, *46*, 8816.
[24] C. G. Hardy, J. Y. Zhang, Y. Yan, L. X. Ren, C. B. Tang, *Prog. Polym. Sci.* **2014**, *39*, 1742.
[25] P. G. Pickup, *J. Mater. Chem.* **1999**, *9*, 1641.
[26] B. Dong, D. Y. Zhong, L. F. Chi, H. Fuchs, *Adv. Mater.* **2005**, *17*, 2736.
[27] X. Mao, W. Tian, J. Wu, G. C. Rutledge, T. A. Hatton, *J. Am. Chem. Soc.* **2015**, *137*, 1348.
[28] A. B. Kaiser, *Adv. Mater.* **2001**, *13*, 927.
[29] M. Kruk, M. Jaroniec, *Chem. Mater.* **2001**, *13*, 3169.
[30] D. P. Dubal, S. H. Lee, J. G. Kim, W. B. Kim, C. D. Lokhande, *J. Mater. Chem.* **2012**, *22*, 3044.
[31] Y. M. Cui, Z. Y. Wen, X. Liang, Y. Lu, J. Jin, M. F. Wu, X. W. Wu, *Energy Environ. Sci.* **2012**, *5*, 7893.
[32] L. Y. Chang, C. T. Li, Y. Y. Li, C. P. Lee, M. H. Yeh, K. C. Ho, J. J. Lin, *Electrochim. Acta* **2015**, *155*, 263.
[33] S. S. Shinde, G. S. Gund, D. P. Dubal, S. B. Jambure, C. D. Lokhande, *Electrochim. Acta* **2014**, *119*, 1.
[34] K. G. Neoh, E. T. Kang, K. L. Tan, *J. Phys. Chem. B* **1997**, *101*, 726.
[35] C. M. Woodbridge, D. L. Pugmire, R. C. Johnson, N. M. Boag, M. A. Langell, *J. Phys. Chem. B* **2000**, *104*, 3085.
[36] P. G. Gassman, D. W. Macomber, J. W. Hershberger, *Organometallics* **1983**, *2*, 1470.
[37] M. Barber, J. A. Connor, L. M. R. Derrick, M. B. Hall, I. H. Hillier, *J. Chem. Soc., Faraday Trans. 2* **1973**, *69*, 559.
[38] C. Yang, P. Liu, T. Wang, *ACS Appl. Mater. Interfaces* **2011**, *3*, 1109.
[39] W.-H. Qu, Y.-Y. Xu, A.-H. Lu, X.-Q. Zhang, W.-C. Li, *Bioresour. Technol.* **2015**, *189*, 285.
[40] D. Z. Zhu, Y. W. Wang, L. H. Gan, M. X. Liu, K. Cheng, Y. H. Zhao, X. X. Deng, D. M. Sun, *Electrochim. Acta* **2015**, *158*, 166.
[41] H. L. Li, L. X. Jiang, Q. L. Cheng, Y. He, V. Pavlinek, P. Saha, C. Z. Li, *Electrochim. Acta* **2015**, *164*, 252.
[42] S. Balasubramanian, P. Kamatchi Kamaraj, *Electrochim. Acta* **2015**, *168*, 50.
[43] C. H. Kim, B. H. Kim, *J. Power Sources* **2015**, *274*, 512.

[44] V. Khomenko, E. Frackowiak, F. Béguin, *Electrochim. Acta* **2005**, *50*, 2499.
[45] M. D. Stoller, R. S. Ruoff, *Energy Environ. Sci.* **2010**, *3*, 1294.
[46] M. D. Stoller, S. Park, Y. Zhu, J. An, R. S. Ruoff, *Nano Lett.* **2008**, *8*, 3498.
[47] W. C. Jiang, D. S. Yu, Q. Zhang, K. L. Goh, L. Wei, Y. L. Yong, R. R. Jiang, J. Wei, Y. Chen, *Adv. Funct. Mater.* **2015**, *25*, 1063.
[48] B. Dunn, H. Kamath, J. M. Tarascon, *Science* **2011**, *334*, 928.
[49] J. Zhao, S. Xu, K. Tschulik, R. G. Compton, M. Wei, D. O'Hare, D. G. Evans, X. Duan, *Adv. Funct. Mater.* **2015**, *25*, 1616.
[50] Y. J. Peng, T. H. Wu, C. T. Hsu, S. M. Li, M. G. Chen, C. C. Hu, *J. Power Sources* **2014**, *272*, 970.
[51] W. K. Chee, H. N. Lim, I. Harrison, K. F. Chong, Z. Zainal, C. H. Ng, N. M. Huang, *Electrochim. Acta* **2015**, *157*, 88.
[52] Y. L. Zhu, K. Y. Shi, I. Zhitomirsky, *J. Power Sources* **2014**, *268*, 233.
[53] P. X. Li, Y. B. Yang, E. Z. Shi, Q. C. Shen, Y. Y. Shang, S. T. Wu, J. Q. Wei, K. L. Wang, H. W. Zhu, Q. Yuan, A. Y. Cao, D. H. Wu, *ACS Appl. Mater. Interfaces* **2014**, *6*, 5228.
[54] H. X. Feng, B. Wang, L. Tan, N. L. Chen, N. X. Wang, B. Y. Chen, *J. Power Sources* **2014**, *246*, 621.
[55] G. F. Chen, Y. Z. Su, P. Y. Kuang, Z. Q. Liu, D. Y. Chen, X. Wu, N. Li, S. Z. Qiao, *Chem. Eur. J.* **2015**, *21*, 4614.
[56] X. Y. Cai, S. H. Lim, C. K. Poh, L. F. Lai, J. Y. Lin, Z. X. Shen, *J. Power Sources* **2015**, *275*, 298.
[57] M. Shao, Z. Li, R. Zhang, F. Ning, M. Wei, D. G. Evans, X. Duan, *Small* **2015**, *11*, 1613.
[58] W. C. Chuan Xia, X. Wang, M. N. Hedhili, N. Wei, H. N. Alshareef, *Adv. Energy Mater.* **2015**, *5*, 1614.
[59] T. Liu, L. Finn, M. Yu, H. Wang, T. Zhai, X. Lu, Y. Tong, Y. Li, *Nano Lett.* **2014**, *14*, 2522.
[60] C. Meng, C. Liu, L. Chen, C. Hu, S. Fan, *Nano Lett.* **2010**, *10*, 4025.
[61] E. Frackowiak, *Phys. Chem. Chem. Phys.* **2007**, *9*, 1774.
[62] G. Wang, L. Zhang, J. Zhang, *Chem. Soc. Rev.* **2012**, *41*, 797.
[63] H.-S. Qian, S.-H. Yu, L.-B. Luo, J.-Y. Gong, L.-F. Fei, X.-M. Liu, *Chem. Mater.* **2006**, *18*, 2102.
[64] L. Zhang, G. Zhang, H. B. Wu, L. Yu, X. W. Lou, *Adv. Mater.* **2013**, *25*, 2589.
[65] M.-M. Titirici, M. Antonietti, *Chem. Soc. Rev.* **2010**, *39*, 103.
[66] W.-M. Zhang, J.-S. Hu, Y.-G. Guo, S.-F. Zheng, L.-S. Zhong, W.-G. Song, L.-J. Wan, *Adv. Mater.* **2008**, *20*, 1160.
[67] H. Zheng, T. Zhai, M. Yu, S. Xie, C. Liang, W. Zhao, S. C. I. Wang, Z. Zhang, X. Lu, *J. Mater. Chem. C* **2013**, *1*, 225.
[68] R.-J. Roe, *Methods of X-ray and Neutron Scattering in Polymer Science*, Oxford University Press, New York **2000**.
[69] X. W. Mao, G. C. Rutledge, T. A. Hatton, *Langmuir* **2013**, *29*, 9626.
[70] C. I. Simionescu, I. Cianga, M. Ivanoiu, A. Airinei, M. Grigoras, I. Radu, *Eur. Polym. J.* **1999**, *35*, 1895.
[71] V. A. Karachevtsev, A. M. Plokhotnichenko, M. V. Karachevtsev, V. S. Leontiev, *Carbon* **2010**, *48*, 3682.
[72] S. Salahi, M. S. Iashkenari, M. Abbaszadeh, M. Pousti, M. Ghorbani, *Synth. Met.* **2014**, *197*, 154.
[73] L. H. Guan, Z. J. Shi, M. X. Li, Z. N. Gu, *Carbon* **2005**, *43*, 2780.
[74] G. Wittstock, H. Emons, W. R. Heineman, *Electroanalysis* **1996**, *8*, 143.
[75] E. Turkmen, S. Z. Bas, H. Gulce, S. Yildiz, *Electrochim. Acta* **2014**, *123*, 93.